16-Way Ka-Band Power Combiner Using Novel Waveguide Transitions

Philipp Neininger, Martin Zink, Laurenz John, Christian Friesicke, *Member, IEEE*, Axel Tessmann, Rüdiger Quay, *Senior Member, IEEE*, and Thomas Zwick, *Fellow, IEEE*

***Abstract*— In this article, we present the design, manufacturing, and experimental validation of a Ka-band wide-bandwidth and low-loss 16-way combiner. We specifically focus on the analysis and demonstration of the combiner's suitability for operation at millimeter-wave (mmW) frequencies. To that end, we extend the established radial-combiner design procedure. As part of this, we propose an oversized feeder design that allows for exceptional insertion and return loss. Furthermore, for the first time, we introduce a peripheral transition from the radial line to rectangular waveguide with integrated matching network and suitable schematic models. We also explore the design space of the radial line itself by analyzing the properties of various height tapers and, as a result, introduce an optimized radial-line profile that minimizes its reflections. The demonstrator measurements indicate an insertion loss (IL) of less than 0.24 dB, a return loss of better than 17 dB, and a phase imbalance of less than 3° in the entire Ka-band. To the best of the authors' knowledge, this is the lowest IL for a wideband multiway combiner and at the same time one of the most broadband combiner solutions realized in the Ka-band.**

***Index Terms*— Ka-band, millimeter-wave (mmW) devices, radial power combiner, spatial combiner.**

I. Introduction

In THE area of microwave and millimeter-wave (mmW) systems, there are many applications requiring high output power, some of them over a wide bandwidth. In the past and to a degree to this day, many of these applications have been addressed using vacuum tube devices, such as traveling-wave tube amplifiers (TWTAs). However, in recent years, the development of solid-state high-power amplifiers (SSPAs) has led to devices with a high output power density and reasonable efficiencies, often realized using the gallium nitride (GaN) technology [1]. The power levels achieved by these monolithic microwave integrated circuits (MMICs) are similar to what previously could only be produced by TWTAs and similar devices. Moreover, to further increase the available power levels, a variety of approaches to combine the output power of multiple devices have been developed.

These power-combining approaches can be divided into two major groups: the corporate and the axially symmetric combiner. Other concepts, such as the traveling-wave combiner, will not be considered here as they are exceedingly difficult to realize for a large number of constituent amplifiers n. The corporate combiner comprises a number of forks, where the power of two inputs is merged into one output. Thus, in a corporate structure comprising n amplifiers, the signal will pass $\log_2 n$ fork unit cells and the conductors connecting them. As can readily be calculated, a large portion of the system losses accrue in the connections between the forking stages [2]. In particular, for larger n, this type of combiner is therefore preferably realized in waveguide technology, as has been shown in the Ka-band for $n = 32$ by Epp *et al.* [3]. Other publications target an improved bandwidth performance [4] or higher operating frequencies [5], [6] up to G-band [7].

While corporate combiners can be realized as a 2-D structure, axially symmetric combiners exploit the third dimension to centrally feed the signal and employ a division network that connects to an arbitrary number of equidistant peripheral ports. This leads to a substantially reduced signal path length and can thus result in lower insertion loss (IL). The means by which the electromagnetic (EM) wave is split and guided has evolved considerably since Wilkinson [8] pioneered a 16-way coaxial divider in 1960. Instead of using a single $\lambda/4$ line for impedance matching, recent coaxial combiner publications feature carefully designed tapered impedance transformers [9], [10]. For an additional doubling in the number of unit amplifiers, Jia and York [11] and Jia *et al.* [12] combined this concept with fin line tapers. Other exceptionally broadband combiner solutions were demonstrated using ridge waveguides as peripheral ports [13], [14].

Axially symmetric combiners can also be constructed using a circular waveguide as the central port, with rectangular waveguides (RWGs) directly feeding this central cavity (circular waveguide combiners). In the most common implementation, the combined energy travels in the $TE_{01,circ}$ circular waveguide mode and is coupled to a standard RWG using a mode transducer. This concept was demonstrated by Chen [15] using a Marié mode transducer. Recently, Chu *et al.* [16]

Manuscript received January 11, 2022; revised March 7, 2022; accepted March 26, 2022. Date of publication April 28, 2022; date of current version June 3, 2022. This work was supported in part by the Federal Office of Bundeswehr Equipment, Information Technology and In-Service Support (BAAINBw) through the Project Subsys and in part by the Research Fab Microelectronics Germany (FMD) funded by the Federal Ministry of Education and Research (BMBF). *(Corresponding author: Philipp Neininger.)*

Philipp Neininger, Martin Zink, Laurenz John, Christian Friesicke, Axel Tessmann, and Rüdiger Quay are with the Fraunhofer Institute for Applied Solid State Physics (Fraunhofer IAF), 79108 Freiburg, Germany (e-mail: philipp.neininger@iaf.faunhofer.de).

Thomas Zwick is with the Institute of Radio Frequency Engineering and Electronics (IHE), Karlsruhe Institute of Technology (KIT), 76131 Karlsruhe, Germany.

Color versions of one or more figures in this article are available at https://doi.org/10.1109/TMTT.2022.3166178.

Digital Object Identifier 10.1109/TMTT.2022.3166178

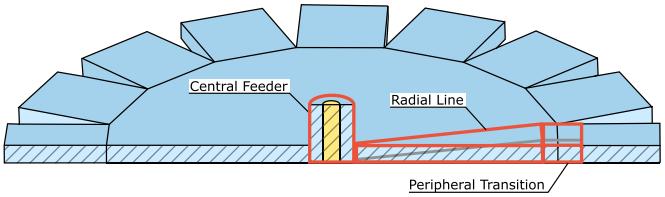

Fig. 1. Isometric projection and cross section of a generic radial-line power combiner. The system can be divided into three principal components: the central feeder, the radial line, and the peripheral transition.

improved the design by introducing a new mode transducer that is considerably more compact and exhibits lower IL than previous designs. In addition, a similar structure that employs the $TM_{01,circ}$ mode instead was recently shown by Montejo-Garai *et al.* [17] to achieve an improved efficiency at *X*-band.

Another group of topologies to be outlined in this context is using a coaxially fed radial line, labeled radial-line combiner in this work. While the radial line itself was described by Marcuvitz [18], Schellenberg and Cohn [19] introduced a 12-way combiner at *X*-band using a quartz substrate as a radial line. The concept was applied by other authors with different numbers of peripheral ports in the following decades. Subsequently, Belohoubek *et al.* [20] demonstrated a 30-port *X*-band design. Furthermore, the operating frequency was shown to be scalable well into the *W*-band by Schellenberg *et al.* [21], [22].

Although there are publications analyzing the design procedure and electrical behavior of the radial-line combiner, they are limited to a quartz-substrate radial line [2] or to coaxial input–output connectors [23]. However, as the operating frequency of high-power semiconductors increases, those concepts become difficult to employ without accumulating excessive IL. It is therefore beneficial to analyze each of the combiner's components carefully and extend the established design procedure to be scalable to high-power, high-frequency designs while using low-loss waveguide interfaces as much as possible.

In this article, we therefore develop an enhanced design procedure that builds on a novel analysis of the radial-line combiner system to address the requirements outlined above. We specifically focus on IL, bandwidth, and applicability at mmW frequencies. Fig. 1 shows an overview of a generic radial-line combiner—each of the three major components shown is examined and optimized in Section II. This includes the development of a significantly improved peripheral transition from radial line to RWG in Section II-D, a novel exploration of various radial-line cross sections in Section II-A, and vital system considerations in Section II-F. Furthermore, measurement results of the system demonstrator are presented in Section III. A comparison to the state of the art will be given in Section IV and a conclusion can be found in Section V.

II. Combiner System Analysis

In this section, a detailed design procedure for a radial-line combiner system will be presented, which extends the procedure detailed in [2] to higher frequencies and various

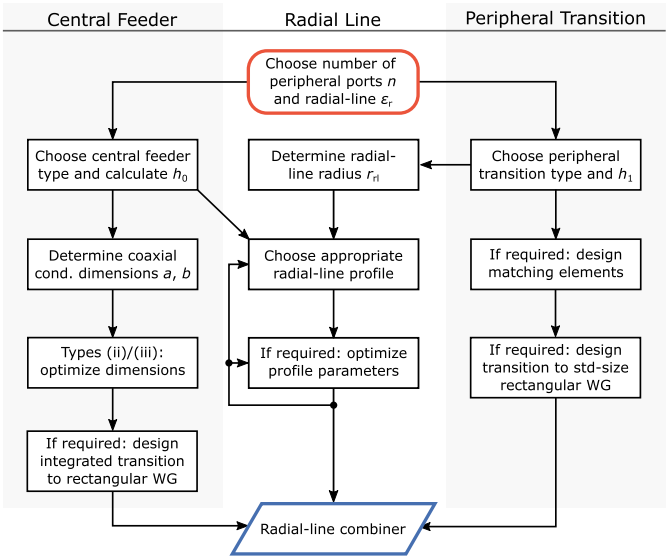

Fig. 2. Generalized design process for a radial-line combiner. It can be divided into three partly independent subtasks: design of the central and peripheral transitions and design of the radial line.

interconnects. It is summarized in Fig. 2. From an EM standpoint, a radial-line combiner can be divided into three main parts. As seen from the power sources, a peripheral transition is the first component. It connects the source to the radial line, which is the second component and guides the source power toward the center. Finally, a central feeder collects the signal power in the center of the radial line and provides a common output port. An illustration of a general configuration is shown in Fig. 1. All three components can be realized using different concepts, as will be outlined in this section.

A. Radial-Line Design Space

The first step in designing the radial line (c.f. Fig. 2) is to determine its radius, r_{rl}. This value depends on the number of peripheral ports n and the width of a single peripheral transition d (as detailed in Section II-D). Approximating the n-sided polygon as a circle leads us to require at least a radial-line circumference of $C = n \cdot d$. Its radius then equates to

$$r_{rl} = \frac{n \cdot d}{2\pi}. \tag{1}$$

In general, a radial line can be modeled as a parallel-plate transmission line that expands in width as the wave travels outward from the center to the n peripheral ports. From the impedance relation of a parallel-plate line [24], we thus have for the nth part of a radial line [25]

$$Z_{0,rl}(r) = \frac{hn}{2\pi r} \cdot \sqrt{\frac{\mu}{\epsilon}} \tag{2}$$

where h is the line height and r is the line radius.

As can be seen from (2), the characteristic impedance $Z_{0,rl}$ varies strongly over the line radius. This property is shown by the dotted curve in Fig. 3(b). In case of an even-mode

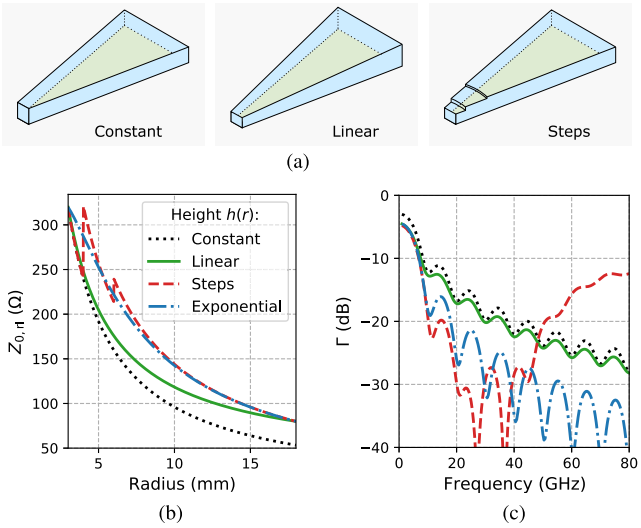

Fig. 3. Various radial-line height profiles, their respective impedance functions over radius, and reflection coefficients versus frequency. (a) Various radial-line height profiles, (b) their respective impedance functions over radius, and (c) reflection coefficients versus frequency.

excitation, only the TEM mode is able to propagate in the radial line. Therefore, we can use analytical solutions for nonuniform transmission lines as described by Bergquist [26] to determine the reflection coefficients Γ of the line without EM simulation. The dotted curve in Fig. 3(c) shows the resulting Γ calculated using Bergquist's algorithm with the line split into 2001 constant-impedance segments of equal length. As can be seen, it shows a high-pass behavior and rather large reflection coefficients for lower frequencies.

However, in (2), there is an additional degree of freedom in the radial-line plate distance $h(r)$, which we propose to exploit to improve the radial line's reflection coefficient. To that end, we investigated the properties of various height profiles, three of which are shown in Fig. 3(a).

Apart from the constant-height profile, we considered a linear and an exponential height taper and a stepped-height layout. The exponential curve was drawn using

$$h(r) = h_1 - h_\Delta \cdot \exp\left(-k \cdot (r - r_0)\right) \tag{3}$$

with the peripheral-port height h_1 and the height difference $h_\Delta = h_1 - h_0$. On the other hand, the stepped profile features two steps of variable height and variable placement. Finally, the linear taper features a height gradient between the central-port height h_0 and the peripheral-port height h_1.

Using Bergquist's algorithm, we can efficiently optimize the profiles' variables, such as the step height ratio s, the step locations r_{s0} and r_{s1}, or the exponential growth factor k. We applied this optimization for the Ka-band frequency range using a custom Python script, which resulted in the values shown in Table I.

From the reflection coefficients shown in Fig. 3(c), we can see little difference between the constant and linear profiles, both are above -20 dB up to 37 GHz. In comparison, the exponential profile exhibits a substantial improvement—the highest simulated reflection coefficient being below -20 dB.

TABLE I
RADIAL-LINE COMBINER: REALIZATION PARAMETERS

Property	Symbol	Value
Step height ratio	s	0.678
First step radius	r_{s0}	4.0 mm
Second step radius	r_{s1}	6.0 mm
Radial line central-port height	h_0	1.0 mm
Radial line peripheral-port height	h_1	1.5 mm
Exponential growth factor	k	$500\,\mathrm{m}^{-1}$
Number of peripheral ports	n	16
Radial line outer radius	r_{rl}	18 mm
Radial line substrate perm.	ϵ_{r}	1
Coaxial section length	l_{c}	8.5 mm
Coaxial line inner radius	a	0.7 mm
Coxial line outer radius	b	1.7 mm
Peripheral port width	d	7.112 mm

The growth factor k in (3) turns out to be optimal around 500. For higher values, the sharp gradient leads to higher reflections again. In contrast to the high-pass characteristics of the other profiles, the optimized stepped profile exhibits a bandpass behavior with a reflection coefficient below -25 dB in the Ka-band.

The exponential profile, especially for very high growth factors k, generates a complex height gradient in the center region. From a manufacturing standpoint, this is more intricate to realize as opposed to a stepped profile with piecewise constant height. Furthermore, the stepped profile's superior reflection coefficient makes it a great solution even for medium-to-high-bandwidth systems, e.g., covering one RWG band. For systems covering multiple octaves, the exponential profile could be preferred.

B. Central Feeder

To feed the radial line evenly, a field distribution exhibiting axial symmetry is required, which is fulfilled by a coaxial TEM mode. The first parasitic mode in a coaxial line is designated TE_{11} and occurs at $f_{c,\mathrm{TE11}}$. Thus, using

$$(a+b) \approx \frac{c_0}{\pi\sqrt{\epsilon_r} \cdot f_{c,\mathrm{TE11}}} \tag{4}$$

where a and b are the coaxial inner and outer conductor radii, respectively [24, p. 132], and we can determine the upper boundary of the coaxial dimensions. For this design, we require a maximum operating frequency of 40 GHz, so we obtain $(a+b) \leq 2.39$ mm. Setting a to 0.7 mm and b to 1.7 mm results in a coaxial line with $Z_0 = 53.2\ \Omega$ and a TE_{11} cutoff frequency of 40.6 GHz.

In general, three types of central feeders can be distinguished, as shown in Fig. 4(a). For type (i), the coaxial inner conductor is directly attached to the radial bottom plate, while the outer conductor connects to the top plate [27]. For electrically large values of h_0, this type suffers from rather large return loss values, as shown in Fig. 4(b).

As the IL and power handling capability depend on h_0, it is advantageous to choose an electrically large value. Type (ii) includes a capacitive compensation to allow for this and

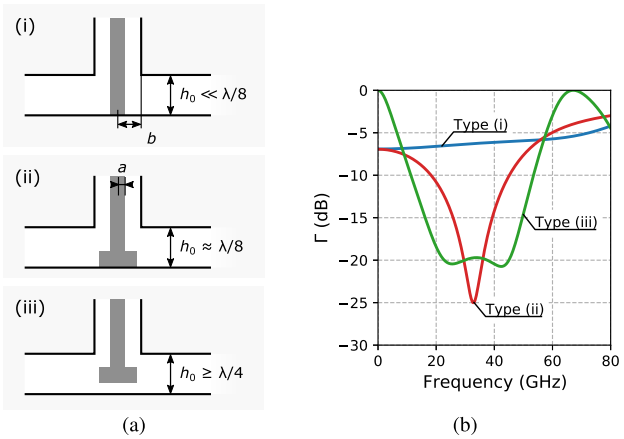

Fig. 4. Cross sections and reflection coefficients for three feeder variants of increasing manufacturing complexity. (i) Plain coaxial line. (ii) Coaxial line with capacitive compensation. (iii) Suspended disk probe. Note that the *S*-parameters are referenced to the nonnormalized port impedances. (a) Cross sections. (b) Reflection coefficients for three feeder variants.

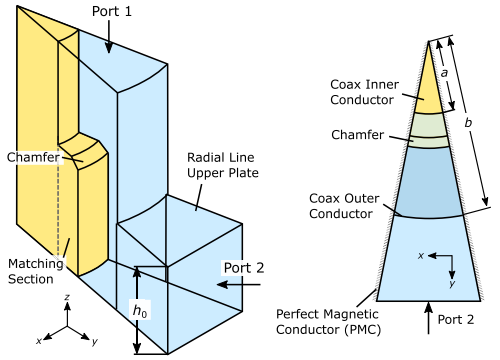

Fig. 5. Perspective view and top projection of a 1/16 coaxial line and the type (ii) central feeder to the radial-line structure. The PMC face boundary condition on both sides of the model increases the impedance level by a factor of 16 and decreases simulation times significantly.

simultaneously achieve significant improvements in return loss and bandwidth. It features an increase of the inner conductor radius in the vicinity of the feeder [28]. Given ϵ_r and the maximum operating frequency $f_{\max}$, h_0 for type (ii) can be approximated using

$$h_0 \approx \frac{c_0}{8\sqrt{\epsilon_r} \cdot f_{\max}}. \tag{5}$$

The third feeder type (iii) shown in Fig. 4(a) features a disk-shaped probe that is suspended in the interface between coaxial and radial lines [29]. In comparison to type (ii), this topology contains an additional degree of freedom in the disk height above the lower radial plate. Since it requires an auxiliary structure to mount on, it possesses the highest manufacturing complexity. In past publications [30], mounting has been resolved by attaching the disk via a PTFE dielectric retainer. Type (iii) requires the largest central-port height of $h_0 \geq \lambda/4$ and offers the best return loss and bandwidth of the three approaches, as shown in Fig. 4(b).

To evaluate and optimize the dimensions of the feeder approaches, an efficient simulation model is crucial. An illustration of a model for type (ii) is shown in Fig. 5 (and trivial to adapt to types (i) and (iii)). As before, we can exploit the structure's axial symmetry and consider only its nth fraction. The perfect magnetic conductor (PMC) boundary condition on the symmetry planes ensures that only the desired even TEM mode is propagating and allows for significantly reduced simulation times.

The EM simulation indicates that sharp edges around the center conductor locally increase the electric field strength appreciably. To mitigate this effect, we included a chamfer by 0.1 mm, as shown in Fig. 5. Also, further improving the return loss, the upper edge of the matching section is positioned by 0.5 mm above the upper plate of the radial line.

As a result of these optimizations, feeder type (ii) offers the most favorable compromise between power handling capability, return loss, and manufacturing complexity. In comparison, while transition (iii) exhibits an additional design parameter (disk height) and allows for better return loss, it is also more complex to manufacture and can be difficult to mount inside the radial cavity. The realized structure of type (ii) exhibits a reflection coefficient of below -15 dB in the Ka-band frequency range.

C. Feeder-Integrated Waveguide Transition

All the feeder approaches introduced in Section II-B end in a coaxial line. However, an RWG is a far more suitable choice for mmW power transmission, especially for high-power systems. Therefore, we extended the central feeder to integrate a transition to standard RWG. In this way, the rather lossy coaxial TEM section can be kept as short as possible and no interconnections on the coaxial plane are necessary.

The transition from the oversized coaxial line to RWG has been developed by starting with a plain E-field probe layout similar to [31]. The original design consists of a coaxial line that is inserted into the broad wall center of an RWG, with the coaxial center conductor extended into the waveguide body. While this design works well with smaller coaxial-line radii, it exhibits a parallel resonance when used with the oversized coaxial line within the upper band between 35 and 38 GHz, depending on the exact dimensions used.

At this resonance frequency, a large portion of the energy passes the transition to the coaxial line in the TE_{11} mode pattern [see inset of Fig. 6(e)]. When fed to the radial line, this mode will generate a severely asymmetrical power distribution. As shown in Fig. 6(e), the mode is attenuated below $f_{c,\mathrm{TE11}}$. Nevertheless, a significant amount of energy is reflected and dissipated at the respective frequency. To prevent this, we considered rectangular microstrip transitions, which in principle can generate a very wideband matching response [32]. By introducing a rectangular T-shaped probe tip to our model [c.f. Fig. 6(a)], a similar frequency behavior to that of a plain probe could be simulated [T shape in Fig. 6(c)]. In this case, at 37.6 GHz, a spike in the return loss coincides with a strong deterioration of the IL. This is also reflected in Fig. 6(d), which depicts the mode conversion from the fundamental TE_{10} at the RWG to the high-order TE_{11} at the coaxial interface.

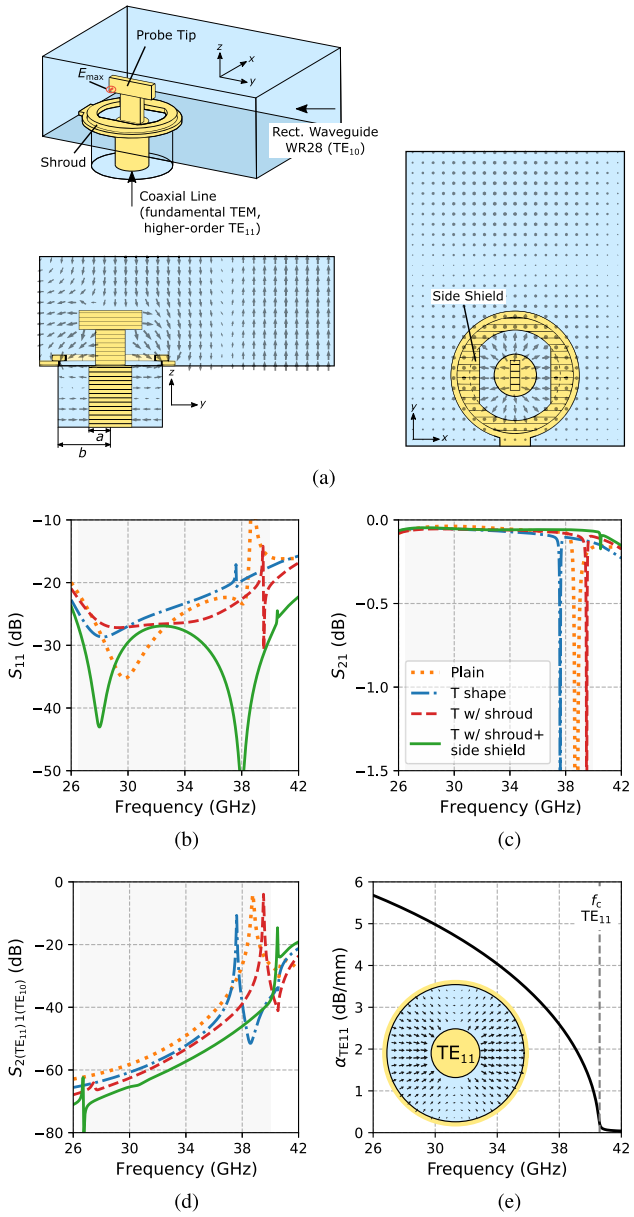

Fig. 6. (a) Perspective views and (b)-(e) EM-simulation results of the feeder-integrated RWG transition. The plots illustrate the effect of the features introduced in Section II-C: a plain version, one using a shroud, and one with both a shroud and the side shield. Both elements move the resonance to higher frequencies and improve the return loss. Furthermore, they decrease the mode conversion to the parasitic coaxial TE_{11} mode [c.f. (c)]. (b) S_{11}. (c) S_{21}. (d) Mode Conversion TE_{10} to TE_{11}. (e) Coaxial TE_{11} attenuation.

However, because this probe is significantly thinner compared to the coaxial inner conductor used in the plain probe, we can restrict the aperture at the top of the coaxial line without coming too close to the outer conductor. The first stage of this concept is highlighted as shroud in Fig. 6(a) and yields an improvement in the resonance frequency by 2 GHz [c.f. Fig. 6(b) and (c)]. In an attempt to further approximate a microstrip-to-waveguide transition, we propose to include a side shield. This feature blocks most of the TE_{11} field components and also improves the return loss of the structure. Combining both of these measures, we obtain a transition with high TEM mode purity in the entire Ka-band. In Fig. 6(c), the resulting S-parameters indicate an IL of less than 0.1 dB, while the simulated resonance is now at 40.5 GHz. The mode conversion plot also shows significantly less coupling to the parasitic TE_{11} mode and equivalently shifted resonances.

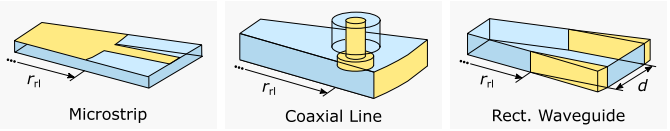

Fig. 7. Three possible implementations of peripheral transitions to connect a power source (right side) to the nth part of a radial line (left side) using microstrip, coaxial line, or RWG.

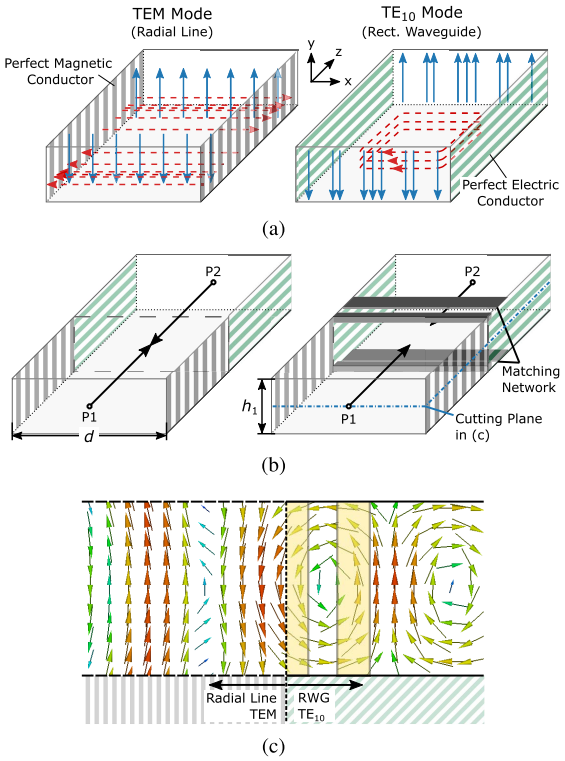

Fig. 8. (a) Two modes involved in the transition from radial line to RWG. (b) Simulation model to characterize the electrical behavior of the mode conversion. (c) H-field in the center of the transition area. The cutting plane location is outlined in (b).

D. Peripheral Transition

The design flow chart's (Fig. 2) right side refers to the design of the peripheral transition, which couples the source energy to the radial line. From Fig. 7, we can see that there are three major approaches to this. Both the transitions to microstrip [2], [20] and coaxial line [23], [25] have been treated thoroughly in the past. As a transition to RWG is best suited for most mmW systems and has not been explored in detail so far, it will be analyzed in the following.

As established in Section II-A, a TEM mode travels inside the radial line. On the other hand, in the target frequency range, the RWG only supports the TE_{10} mode, as shown in Fig. 8(a). For the purposes of this analysis, only the transition

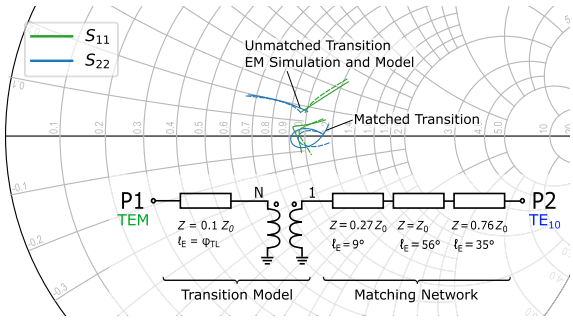

Fig. 9. Smith chart depicting the electrical behavior of the transition from radial waveguide to reduced-height RWG in the frequency range from 27 to 40 GHz. The dashed curves denote model results, while the solid lines pertain to EM simulations.

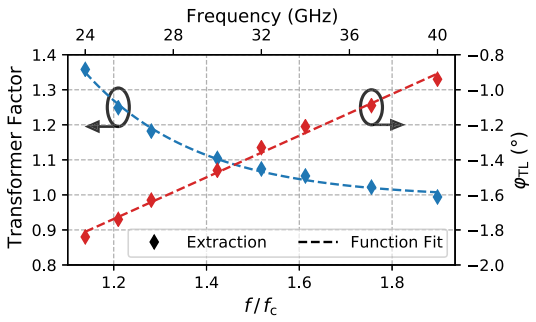

Fig. 10. Peripheral transition between radial line and RWG: equivalent circuit parameters as a function of the RWG cutoff frequency f_c.

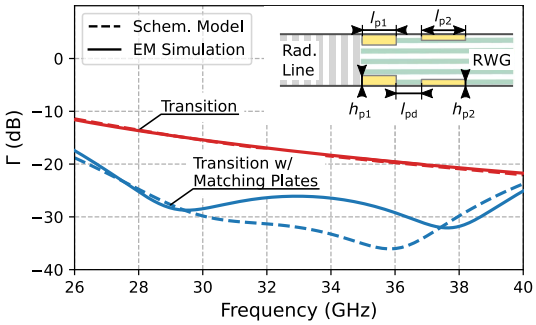

Fig. 11. Reflection coefficient of the peripheral transition from radial line to RWG depicted in Fig. 8(b) with and without the newly developed matching scheme. Inset: cross-sectional view of the transition including the dimensions of the plates for the Ka-band.

area is of interest, and thus, the radial line is approximated as a rectangular box. In it, the E-field (blue) is constant over the x-axis. The PMC boundary condition is used as in Section II-C; this corresponds to an even-mode excitation of the radial line. In contrast to the radial line, the RWG features metallic walls on both sides, which are represented as a perfect electric conductor (PEC) here. Therefore, the E-field is zero at the walls and has its maximum in the center.

Using the simulation model shown in Fig. 8(b), we can characterize the transition between these two modes. The resulting magnetic field in the center of the structure is shown in Fig. 8(c). While on the left, we can see the TEM mode without any field components in the direction of propagation, this characteristic changes at the intersection between the radial line and the RWG (dashed line). On the right of this intersection, the emerging TE_{10} mode features significant H-field components in the direction of propagation.

The Smith chart in Fig. 9 shows the S-parameters of the EM simulation with the reference plane set, as shown by the arrows in Fig. 8(b). Similar to an inductive post [18, p. 221], the transition from PMC to PEC boundary parallel to the electric field causes a frequency-dependent inductive reactance. Unlike with an inductive post, the mode pattern changes from ports 1 to 2, which renders the circuit nonsymmetrical and requires us to use a more complex equivalent circuit.

In Fig. 9, a possible realization of such a transition model equivalent circuit is shown. It consists of a transmission line of electrical length φ_{TL} and characteristic impedance $Z = 0.1\ Z_0$. While the line's characteristic impedance is constant over frequency, its electrical length can be represented by a linear function with

$$\varphi_{TL}(f, d) = 7.93 \times 10^{-9}\ \frac{f \cdot d}{\text{Hz m}} - 3.164 \tag{6}$$

which is shown in red in Fig. 10. Furthermore, we use an ideal transformer with transformer ratio N. The frequency dependency of N resembles an exponential function. A least-squares fit results in the following equation:

$$N(f, d) = 39.52 \cdot \exp\left\{-27.56 \times 10^{-10}\ \frac{f \cdot d}{\text{Hz m}}\right\} + 0.992. \tag{7}$$

The curve fits and the data points that have been extracted by simulation are plotted in Fig. 10. The return loss that this model and the EM simulation exhibit is shown in Fig. 11 (transition), which indicates very close agreement. It turns out that the transition's S-parameters are invariant to changes in the waveguide height and only depend on its width and, therefore, on the cutoff frequency of the TE_{10} mode in the RWG. This is why (6) and (7) only depend on f and the width of the RWG's peripheral port, d. It also enables the model to be used for RWG dimensions other than the Ka-band WR28. Note that even-mode excitation of the radial line is assumed and the radial-line and RWG heights are assumed to be equal.

From the transition model's S-parameters, we can expect a worst case return loss in the range of 12 dB, which would impair the performance of amplifiers that are feeding the combiner considerably. To improve this figure, we propose to implement a transition-integrated matching network. To compensate for the inductive reactance shown in Fig. 9, we use a three-section capacitive-line matching network, a model of which is shown in Fig. 9 (bottom). Optimization using the equivalent circuit leads to the following values: a short low-impedance line of $Z = 0.27\ Z_0$, followed by a longer line of $Z = Z_0$, and another shorter low-impedance line of $Z = 0.76\ Z_0$. The return loss of the model employing lossless transmission lines is shown in Fig. 11 (dashed curve), and the schematic is shown in Fig. 9 (bottom).

To translate this model to the RWG regime, capacitive obstacles are well suited [18, p. 248]. They can be realized by

TABLE II
WAVEGUIDE HEIGHT TRANSFORMER

Symbol	Initial Value	Optim. Value	Rel. Variation
h_1	1.500 mm	—	
h_2	1.739 mm	1.736 mm	0.2 %
h_3	2.310 mm	2.324 mm	0.6 %
h_4	3.067 mm	3.065 mm	0.1 %
h_{WR28}	3.556 mm	—	
l_{tr}	2.914 mm	2.945 mm	1.1 %

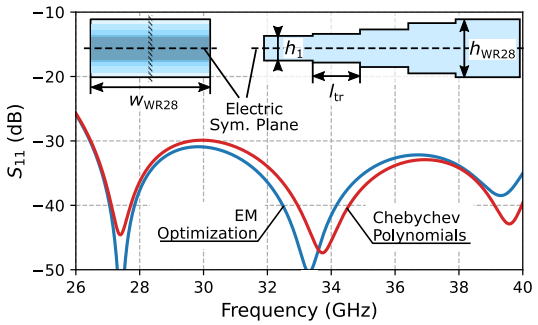

Fig. 12. Front view (left), E-plane cross section (right), and EM-simulated reflection coefficient of the three-section waveguide height transformer from $h_1 = 1.5$ mm to $h_{\mathrm{WR28}} = 3.556$ mm. The dashed and hatched lines (top left) indicate the electric and magnetic symmetry planes, respectively.

introducing plates that are perpendicular to the electric field, as shown in the right of Fig. 8(b). The capacitive reactance introduced is a function of the plate thickness, while the length of the obstacle corresponds to the line length similar to a TEM case. For sufficiently small changes in RWG height, the impedance change can be approximated using [18, p. 307]

$$\frac{Z_a}{Z_b} = \frac{h_a}{h_b}. \tag{8}$$

We employed this approximation to synthesize the plate dimensions. Subsequent EM-simulation-based tuning of the transition yields the blue solid curve in Fig. 11, which is quite close to the model prediction. As can be seen, the newly developed transition exhibits a significantly improved Γ of below -20 dB in the complete Ka-band and is thus ideally suited for use in a wideband low-loss combiner system.

For the Ka-band, the plate lengths l_{p1} and l_{p2} are 0.91 and 1.31 mm, while their heights h_{p1} and h_{p2} amount to 0.24 and 0.08 mm, respectively. The plate-to-plate distance l_{pd} is 1.17 mm (c.f. Fig. 11).

E. Waveguide Height Transformer

If the peripheral transition ends in an RWG as described in Section II-D, the height h_1 [as shown in Fig. 8(b)] depends on various factors and is not necessarily compatible with standardized waveguide equipment. Thus, a low-reflection waveguide height transformer can be crucial, which is explored in this section.

The output of the transition described in Section II-D is an RWG of height $h_1 = 1.5$ mm, while a standard WR28 waveguide flange is significantly higher ($h_{\mathrm{WR28}} = 3.556$ mm). As only the waveguide width determines its lower cutoff frequency, a height transformer can be created similar to an impedance transformer in a TEM case. For small changes in height, an increase in impedance by the same factor results (c.f. (8)). In addition, the discontinuity creates some capacitive shunt reactance. However, for an optimization starting point or small discontinuities, it can be neglected. With this, a Chebyshev transformer can be specified by directly applying the coefficients to the waveguide section heights.

The calculation of Chebychev coefficients is well known and can be found, e.g., in [24, p. 258]. For the three-section case from h_1 to h_{WR28} and a reflection coefficient of $\Gamma_M = -30$ dB, we obtained the values listed in Table II (initial value). The transformer section length is given by a quarter of the guided wavelength at the center-band frequency, $\lambda_g/4 = 2.914$ mm. Fig. 12 shows a simulation model of the structure. On the left, the transformer is depicted as seen from the front. The EM simulation of the model with the dimensions we computed using Chebyshev polynomials produces the red curve in Fig. 12. This is already a satisfactory result and turns out to be near the optimum since subsequent EM optimization, including manufacturing features (roundings due to milling), yields little improvement (blue curve). In Table II, the initial Chebychev and EM-optimized dimensions are listed. As can be seen, the maximum variation is about 1%, which is in the order of typical manufacturing tolerances.

F. Combiner System

A complete radial-line combiner system realized using the previously introduced design flow is shown in Fig. 13(a). In addition to the parts shown, we employ an integrated 90° bend attached to the sum port, allowing us to place a standard waveguide flange on top of the combiner. The simulated reflection coefficient of the structure when excited from the central sum port is shown in Fig. 14(a) (solid curve). As can be seen, it ranges below -19 dB in the Ka-band frequency range. The simulated power division from the sum port to any of the 16 peripheral ports is outlined on the top of Fig. 13(b). Theoretical—that is perfectly balanced and lossless—power division would result in the dashed line at $1/16 = -12.04$ dB for all S_{n1}. In terms of actual power lost due to reflections and ohmic losses, the simulation predicts the values of around 0.23 dB, which equates to a projected efficiency of $\eta = 94.8\%$.

For the final configuration with the dimensions chosen as shown in Table I, the imbalance of the power fractions delivered to the peripheral ports is simulated to be less than 0.05 dB below 38 GHz. A major factor that determines this value is the length of the coaxial line section l_c in Fig. 13(a). Varying l_c, we can extract the maximum and average power imbalance, as shown in Fig. 14(b). For very short l_c below 4 mm, both the average and the maximum power imbalance increase significantly. On the other hand, for very long coaxial line lengths, the simulation suggests almost perfect symmetry, albeit at the cost of a higher IL. However, as pointed out in Section III, the correct alignment of the central conductor is crucial and becomes harder as the coaxial section increases in length. Furthermore, Fig. 14(a) shows that the reflection

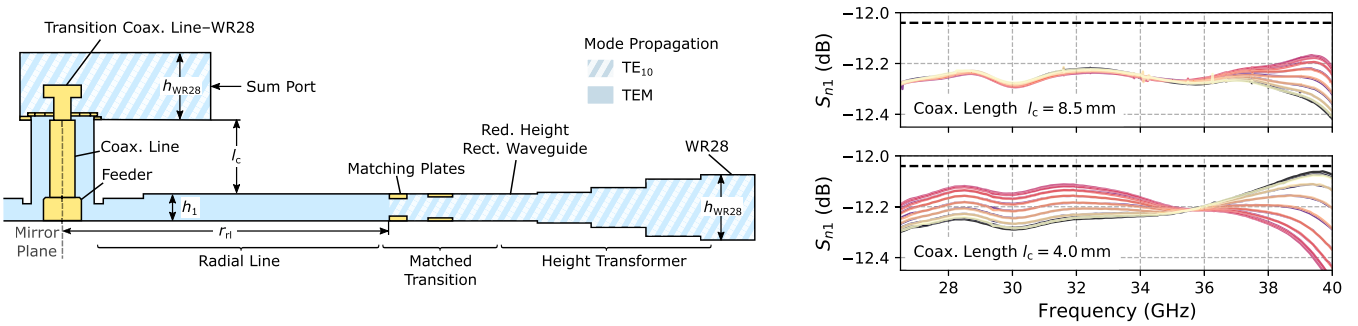

Fig. 13. (a) Cross-sectional view of the developed radial-line combiner system. The mirror plane of the axially symmetric portion is indicated by a dashed line on the bottom left. For brevity, the mirrored left part is not shown. (b) EM-simulated IL toward all 16 divider ports when excited from the sum port for two different coaxial lengths l_c. Neighboring peripheral ports are colored similarly.

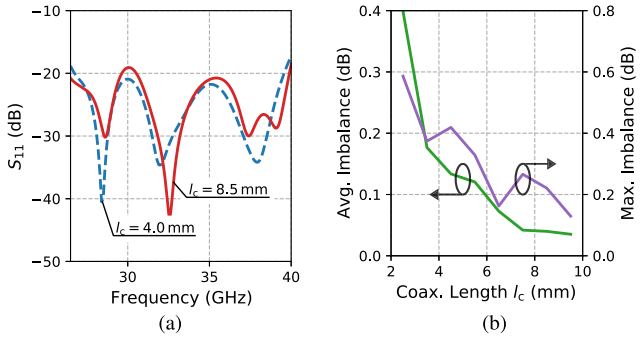

Fig. 14. (a) EM-simulated return loss of the complete combiner assembly as shown in Fig. 13(a) for two different values of l_c (S_{11} magnitude). In both cases, the structure is excited from the sum port and the plots show the power distribution toward all 16 divider ports as well as the central-port return loss in case of terminated peripheral ports. (b) Average and maximum amplitude imbalance versus coaxial line length, l_c.

coefficient changes only slightly with l_c and is thus not a factor in this optimization process.

On closer inspection of the power distribution simulations as shown in Fig. 13(b), we can note that with the short coaxial line section (lower plot), the offset between geometrically opposite ports rises to 0.2 dB for the lower band and to more than 0.4 dB at the upper band edge. Furthermore, at 35.8 GHz, the S_{n1} curve set exhibits a crossover, where the ports that are underpowered in the lower band deliver a higher power in the upper band. This characteristic is a result of two factors.

1) At the lower band edge, only the simulation featuring the short coaxial line [Fig. 13(b)—bottom] shows appreciable asymmetry in the power delivery. This indicates a coupling effect that is present for electrically short distances between the radial line and the sum port RWG.
2) At the upper band edge, both results exhibit degradation in power symmetry, as the central coaxial-to-waveguide transition produces a field pattern that is a superposition of TEM and TE_{11} modes. In addition, the coaxial line's attenuation for the high-order TE_{11}-mode declines as the frequency approaches $f_{c,TE11}$.

In terms of phase deviation (not shown), similar results can be observed in simulation. Excited from the central sum port, the device employing a short coaxial section exhibits a maximum phase imbalance of 3° between output ports. With the optimized value for l_c, this figure drops below 0.8°. In summary, while the longer coaxial section causes slightly higher IL, it is preferred due to its superior symmetry characteristics.

In view of the system's power handling capability, we also inspected the simulated E-field patterns. The field maximum is located within the central integrated transition to RWG, where the probe is closest to the waveguide walls [E_{max} in Fig. 6(a)]. Assuming a breakdown electric field strength of E_{br} = 3 kV/mm in air [24, p. 160], a power handling capability P_{max} of 749.2 W can be calculated.

III. Measurements and Analysis

With the combiner system simulations established in Section II, we constructed and milled a demonstrator unit. It comprises a lower and an upper plate and a sum port assembly, as can be seen from the photograph in Fig. 15(a), and features standard WR28 waveguide interconnects on all ports.

For the following experiments, the demonstrator was populated with waveguide loads on all but the measured ports. Fig. 15(b) shows the magnitude of the 16 individual S_{n1} measurements, where the central sum port is designated as port 1 and the surrounding port numbers increase anticlockwise starting closest to the sum port. The gray dashed line indicates the theoretical maximum value in case of perfectly symmetrical and lossless power distribution toward all ports, S_{n1} = −12.04 dB. The target frequency range (Ka-band) is illustrated by the light-gray background.

As can be seen, the transmission amplitudes are fairly close to the theoretical maximum value in the target band. For frequencies below the target band, a homogeneous decrease in transmission is noticed. On the other hand, above the band edge, a sudden separation of the curves is visible. This effect results from the asymmetrical feeding of the radial line above the band of interest, which is caused by the coaxial feeder. On the other hand, for frequencies below the design band, the deterioration of S_{n1} is only caused by a degradation of the input return loss.

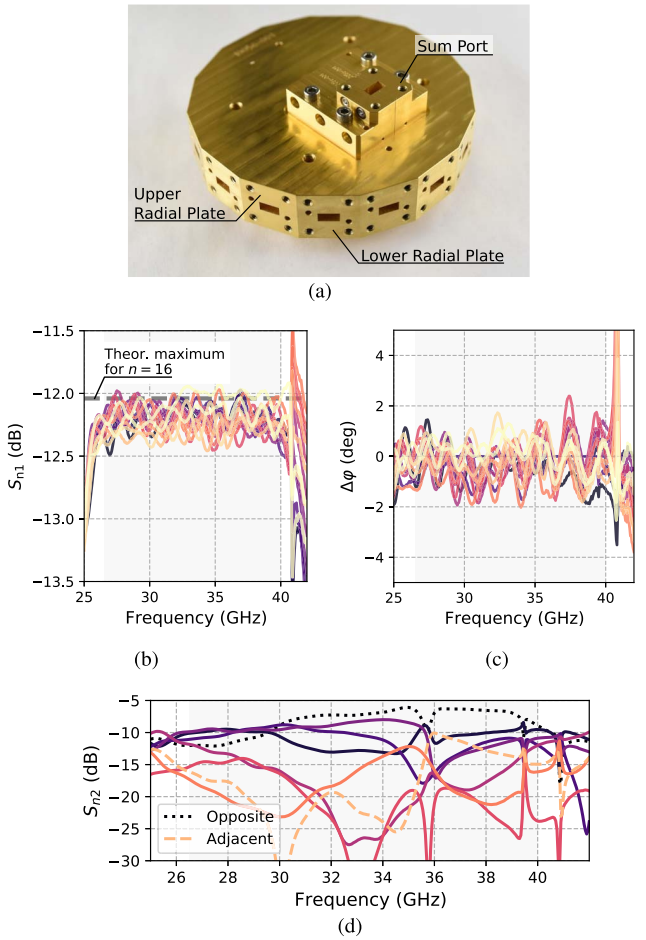

Fig. 15. (a) Assembly photograph and measurement results of the demonstrator's (b) power division (S_{n1} magnitude), (c) insertion phase (S_{n1} phase), and (d) odd-mode isolation characteristics (S_{n2} magnitude). The target band of 26.5–40 GHz is highlighted by a gray background.

Another important metric for a power-combining system is the relative phase offset $\Delta\varphi$ between the peripheral ports [33], which is shown in Fig. 15(c). In the band of interest, the results indicate a maximum phase deviation of 2.2°, which suggests very good uniformity of the structure. Again, above the band edge, the phase offset increases abruptly, which is consistent with the findings detailed above.

Measurement results of the odd-mode isolation between peripheral ports (i.e., S_{n2}) are shown in Fig. 15(d). Due to the combiner's symmetry, only 8 out of 16 curves are shown. With a minimum of 6.9 dB at 35 GHz, the lowest isolation was measured between opposite ports (dotted curve). On the other hand, directly adjacent ports (dashed curve) exhibit a significantly higher isolation of more than 10 dB in the entire measurement range. These rather low values result from the omission of dedicated odd-mode isolation elements and are typical of similar combiner systems. If amplifiers with severely differing insertion phase would be used, load-pulling phenomena could occur, which could deteriorate the power or efficiency of the amplifiers [34]. However, in our own experiments with amplifiers that feature an insertion phase spread of up to ±25°, no significant deterioration could be observed [35].

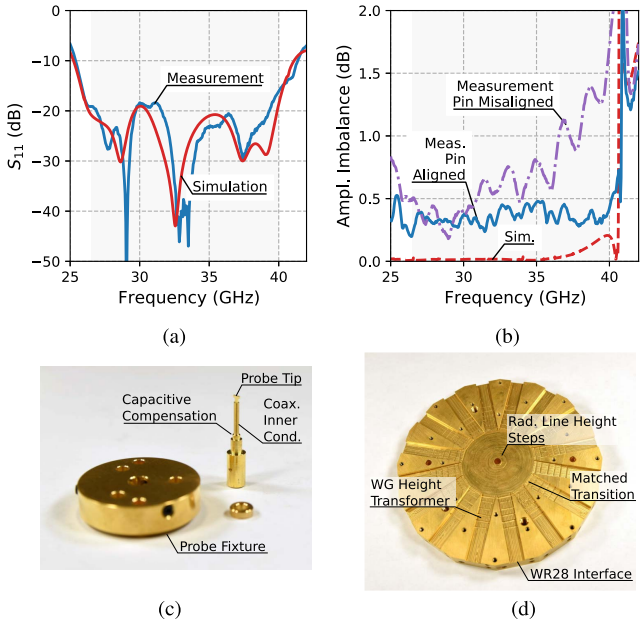

Fig. 16. Measured and simulated reflection coefficient of (a) central sum port and (b) maximum amplitude imbalance of the radial-combiner demonstrator from the central sum port to each of the $n = 16$ peripheral ports. (c) Central feeder assembly that is inserted in the lower radial plate. (d) Top radial plate.

A comparison of the measured and simulated sum-port reflection coefficients can be seen in Fig. 16(a). The simulation predicts a return loss of better than 19 dB in the entire Ka-band. On the other hand, the measured curve shows very similar characteristics. As such, the measured S_{11} amounts to below −18.7 dB for frequencies lower than 39 GHz. Near the upper band edge, it increases to −16 dB at 40 GHz. Of course, slight deviations between measurement and simulation are expected and could be caused by the nonzero reflection of the 15 waveguide loads as well as by the machining tolerances.

During the measurement process, we observed that the correct placement of the coaxial line and probe tip inside the radial plate is critical to achieving symmetrical excitation of the radial line and, thus, the peripheral ports. A photograph of the feeder assembly, which consists of the coaxial inner conductor and attached probe itself and the probe fixture, is shown in Fig. 16(c). During assembly, the probe fixture is used to position the probe inside the split block. It is inserted into and fastened to the lower-plate module and protrudes through the top plate [Fig. 16(d)] into the sum port RWG. To illustrate the impact that variations in placement of the central probe have on the performance of the combiner system, the power imbalance plot shown in Fig. 16(b) is instructive. For each frequency point, it shows the power ratio between the port with the highest and that with the lowest delivered power

$$I(f) = \max(S_{n1,\mathrm{dB}}(f)) - \min(S_{n1,\mathrm{dB}}(f)). \tag{9}$$

The simulation of the structure (dotted line) predicts a power imbalance of close to 0 dB for the lower band. For frequencies above 35 GHz, the simulated imbalance slowly increases up to a value of 0.3 dB at 39.8 GHz. Above the band of interest,

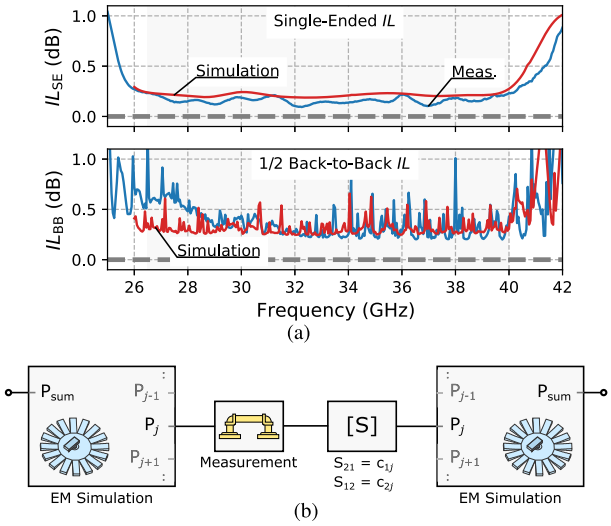

Fig. 17. (a) IL values as calculated by adding the 16-way amplitudes (top) and back-to-back measurement (bottom) and simulation results. (b) Simulation approach used to analyze the back-to-back measurement.

the parasitic high-order modes created by the feeder lead to a sharp increase in electrical asymmetry, which is also indicated by the simulation.

The measured power imbalance is shown by the solid curve in Fig. 16(b). It shows a fairly constant maximum imbalance that ranges between 0.3 and 0.5 dB in the entire band. As we asserted previously, the imbalance sharply increases above 40 GHz and reaches the values above 2 dB.

In contrast, the dashed-dotted curve was acquired with a misaligned feeder assembly, in which the coaxial inner conductor is slightly tilted to one side and thus creates a relatively strong power imbalance in the combiner. This results in a trend of increasing asymmetry with frequency, and the maximum value of 1.7 dB is reached at the upper edge of the band.

A simulation study on the sensitivity of the probe alignment showed that a probe displacement in the aperture of the feeder-integrated waveguide transition [c.f. Fig. 6(a)] of less than 100 μm leads to insignificant changes in the system's RF response. However, for larger displacements approaching 200 μm, an increase of the phase and amplitude imbalance of more than 5° and 0.7 dB occurs, respectively. Also, for significant displacement in parallel to the side shield (x-axis), an increase in the input reflection coefficient of roughly 5 dB was simulated. As a consequence, it can be noted that the alignment of the central feeder assembly is crucial for the proper operation of the combiner system. Via a microscope measurement system, our final alignment was verified to be within ± 20 μm; this was repeatable for several samples.

Finally, in Fig. 17(a), the combiner system's IL is depicted. In the top plot, a comparison of the single-ended IL between measurements and simulation is given, where the values were calculated using

$$\mathrm{IL_{SE}} = 10 \log \sum_{k=2}^{17} |S_{k1}|^2 \tag{10}$$

in which each of S_{k1} represents one individual measurement or is obtained by a 17-port S-parameter file in case of the simulation. We can see that the simulation curve suggests slightly higher losses compared to the measurement—while the simulation averages an IL_{SE} of 0.21 dB in the Ka-band, the measurement yields an average of 0.16 dB and an in-band maximum of 0.23 dB.

On the other hand, in the bottom part of Fig. 17(a), the measurements and simulation of the back-to-back configuration are shown. For this experiment, we had 16 custom U-bends manufactured and connected two of the combiner demonstrators in series. As can be seen, the resulting measurements exhibit a multitude of peaks in which the IL is abruptly increased. In an attempt to find the source of this, we characterized a selection of the U bends separately and found significant insertion phase offsets of 20° between them and an average IL of 0.13 dB.

By replacing the ideal connections in the simulation with a U-bend measurement and an additional phase block as shown in Fig. 17(b), we could replicate this characteristic very closely. The simulation curve at the bottom of Fig. 17(a) shows this simulation, where each connection is assigned a randomly chosen phase offset. Here, we assumed a Gaussian distribution with a standard deviation of $\sigma = 8°$. As a result, we can conclude that the U bends' phase offsets distribution responsible for the peaks encountered in the back-to-back measurement.

With the same simulation setup, we also analyzed the effect of nonreciprocal connections (i.e., $S_{12} \neq S_{21}$) as would be the case if amplifiers were used in the system. Typically, amplifiers exhibit reverse isolation values of 30 dB or more [36]. It turns out that already an S_{12} of -20 dB removes the peak characteristic in the back-to-back simulation (not shown in Fig. 17). Thus, it can be assumed that the single-ended measurement most accurately represents the combiner-induced IL encountered in an SSPA system.

IV. State of the Art

To compare the results shown in this article, it is instructive to consider previous publications of large-scale combiners. A comprehensive overview showing IL and relative bandwidth (RBW) versus center frequency is shown in Fig. 18. It can be seen that IL generally has an increasing tendency for combiners operating toward higher frequencies, while RBW generally decreases with frequency. On closer inspection, several of the publications compiled therein target the Ka-band.

Of these publications, the largest number of sources was reported by Epp *et al.* [3]. With a binary-tree topology, they reached an IL of $\mathrm{IL_{SE}} = 0.7$ dB with 32 source ports from 31 to 36 GHz. More bandwidth (18–40 GHz) has been obtained with a binary tree based on ridge waveguides [4]—this design features an IL of 0.8 dB. Ridge waveguides have also been used in conjunction with radial lines at S-/C- and X-bands, respectively [14], [17]. Another broadband approach is based on a coaxial combiner [10], which reaches an approximate IL of 0.7 dB between 27 and 31 GHz.

A rather narrowband system based on a radial-line combiner was demonstrated in [37]. With 16 source ports, it achieves

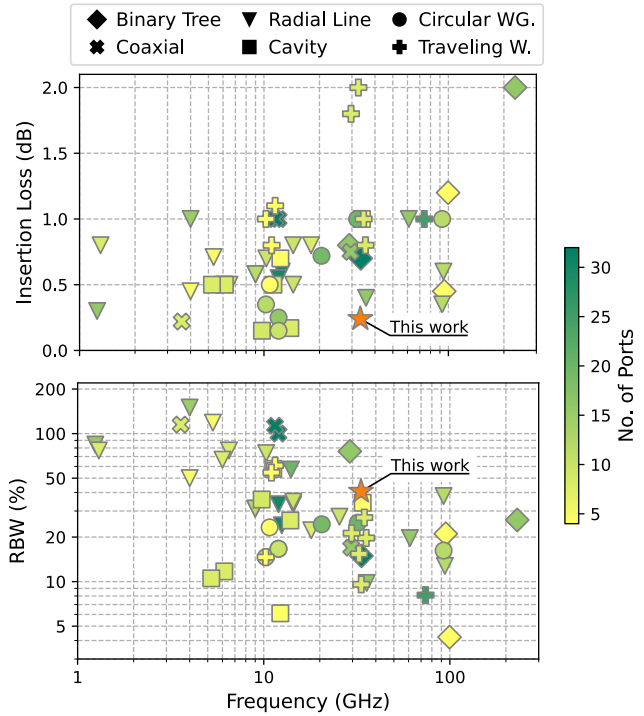

Fig. 18. IL and RBW versus center frequency of large-scale power-combining system publications. The number of ports is shown by the color of the data points.

an IL of 0.3 dB between 35.5 and 36 GHz. Finally, 20- and 24-way combiners employing circular waveguides and mode transducers were demonstrated in [16] and [38], respectively. They show an IL of 1 and 0.6 dB between 28 and 36 GHz, respectively.

Although not in the Ka-band but using a radial-line architecture presumed to be similar to the one shown in this article, several SSPA designs based on radial-line combiners have been demonstrated by Schellenberg *et al.* [21], [22]. Operating in the *W*-band range, they demonstrate broadband matching and an IL of approximately 0.4 dB.

In view of these results, the demonstrator presented in this article stands out by the very low IL in combination with the good return loss over the full Ka-band operating range. It is believed to attain the lowest IL of among all previous large-scale combiners in the Ka-band.

V. Conclusion

In this article, we present the design, analysis, fabrication, and results of a 16-way radial-line combiner in the Ka-band. The main focus of the research is the optimization toward mmW frequencies.

As such, we extend the established design procedure for radial-line combiners to higher frequencies and introduce various new and improved features. To reduce the system IL and increase its power handling capability, we propose an oversized central feeder, which also includes a built-in transition to RWG. We furthermore examine the radial line's EM properties in detail. To that end, we use nonuniform transmission line theory to rapidly compare and optimize several radial-line profiles. In addition, we propose an improved peripheral transition from the radial line to the power sources. By integrating matching plates within the transition area, its return loss is improved significantly. For the first time, this solution provides a simple and wideband waveguide interface for radial-line combiners.

The subsequently fabricated demonstrator's characterization measurements indicate an IL of less than 0.24 dB, a return loss of better than 17 dB, and a port-to-port phase imbalance of less than 3° in the entire Ka-band, which equals an RBW of 40.6%. To the best of the authors' knowledge, this is the lowest IL for a wideband multiway combiner, and at the same time, one of the most broadband combiner solutions realized in the Ka-band.

Acknowledgment

The authors would like to thank the Institute for Applied Solid State Physics' (IAF) Micro Machining Group for the accurate production of the radial combiner.

References

[1] P. Neininger, L. John, P. Bruckner, C. Friesicke, R. Quay, and T. Zwick, "Design, analysis and evaluation of a broadband high-power amplifier for Ka-band frequencies," in *IEEE MTT-S Int. Microw. Symp. Dig.*, Jun. 2019, pp. 564–567.

[2] A. E. Fathy, S.-W. Lee, and D. Kalokitis, "A simplified design approach for radial power combiners," *IEEE Trans. Microw. Theory Techn.*, vol. 54, no. 1, pp. 247–255, Jan. 2006.

[3] L. W. Epp, D. J. Hoppe, A. R. Khan, and S. L. Stride, "A high-power Ka-band (31–36 GHz) solid-state amplifier based on low-loss corporate waveguide combining," *IEEE Trans. Microw. Theory Techn.*, vol. 56, no. 8, pp. 1899–1908, Aug. 2008.

[4] Z. Dang, H.-F. Zhu, J. Huang, and H.-D. He, "An ultra-wideband power combining in ridge waveguide for millimeter wave," *IEEE Trans. Microw. Theory Techn.*, vol. 68, no. 4, pp. 1376–1389, Apr. 2020.

[5] B. Kim, T. Phan, and J. Schellenberg, "4W W-band GaN solid-state power amplifier," in *Gov. Microc. Applic. Crit. Technol. Conf.*, 2013, pp. 1–4.

[6] F. Zhang, K. Song, G. Li, and M. Zhao, "Sub-THz four-way waveguide power combiner with low insertion loss," *J. Infr., Millim., THz Waves*, vol. 35, no. 5, pp. 451–457, May 2014.

[7] H. Kazemi *et al.*, "Ultra-compact G-band 16way power splitter/combiner module fabricated through a new method of 3D-copper additive manufacturing," in *IEEE MTT-S Int. Microw. Symp. Dig.*, May 2015, pp. 1–3.

[8] E. J. Wilkinson, "An N-way hybrid power divider," *IRE Trans. Microw. Theory Techn.*, vol. 8, no. 1, pp. 116–118, Jan. 1960.

[9] R. D. Beyers and D. I. L. de Villiers, "A general impedance tapered transition for N-way conical and coaxial combiners," *IEEE Trans. Microw. Theory Techn.*, vol. 64, no. 12, pp. 4482–4490, Dec. 2016.

[10] P. G. Courtney, J. Zeng, T. Tran, H. Trinh, and S. Behan, "120 W Ka band power amplifier utilizing GaN MMICs and coaxial waveguide spatial power combining," in *IEEE Compd. Semiconductor Integr. Circuit Symp.*, Oct. 2015, pp. 1–4.

[11] P. Jia and R. A. York, "A compact coaxial waveguide combiner design for broadband power amplifiers," in *IEEE MTT-S Int. Microw. Symp. Dig.*, May 2001, pp. 43–46.

[12] P. Jia, L.-Y. Chen, A. Alexanian, and R. A. York, "Multioctave spatial power combining in oversized coaxial waveguide," *IEEE Trans. Microw. Theory Techn.*, vol. 50, no. 5, pp. 1355–1360, May 2002.

[13] J. Deng, Q. Wang, Y. Hu, and P. Zhao, "A novel wideband radial waveguide power combiner using coaxial-to-ridge waveguide transitions," *Rev. Sci. Instrum.*, vol. 90, no. 3, Mar. 2019, Art. no. 034701.

[14] M. M. Fahmi, J. A. Ruiz-Cruz, and R. R. Mansour, "Design of ridge waveguide radial combiners," *IEEE Trans. Microw. Theory Techn.*, vol. 70, no. 1, pp. 895–906, Jan. 2022.

[15] M. H. Chen, "A 19-way isolated power divider via the TE_{01} circular waveguide mode transition," in *IEEE MTT-S Int. Microw. Symp. Dig.*, Jun. 1986, pp. 511–513.

[16] Q.-X. Chu, D.-Y. Mo, and Q.-S. Wu, "An isolated radial power divider via circular waveguide TE_{01}-mode transducer," *IEEE Trans. Microw. Theory Techn.*, vol. 63, no. 12, pp. 3988–3996, Dec. 2015.

[17] J. R. Montejo-Garai, J. A. Ruiz-Cruz, and J. M. Rebollar, "A 10-way power divider based on a transducer and a radial junction operating in the circular TM_{01} mode," *IEEE Access*, vol. 7, pp. 127353–127361, 2019.

[18] N. Marcuvitz, *Waveguide Handbook*. Edison, NJ, USA: IET, 1951.

[19] J. Schellenberg and M. Cohn, "A wideband radial power combiner for FET amplifiers," in *IEEE ISSCC Dig. Tech. Papers*, Feb. 1978, pp. 164–165.

[20] E. Belohoubek *et al.*, "30-way radial power combiner for miniature GaAs FET power amplifiers," in *IEEE MTT-S Int. Microw. Symp. Dig.*, Jun. 1986, pp. 515–518.

[21] J. Schellenberg, E. Watkins, M. Micovic, B. Kim, and K. Han, "W-band, 5 W solid-state power amplifier/combiner," in *IEEE MTT-S Int. Microw. Symp. Dig.*, May 2010, pp. 240–243.

[22] J. Schellenberg, A. Tran, L. Bui, A. Cuevas, and E. Watkins, "37 W, 75–100 GHz GaN power amplifier," in *IEEE MTT-S Int. Microw. Symp. Dig.*, May 2016, pp. 81–84.

[23] K. J. Song, F. Zhang, S. Y. Hu, and Y. Fan, "Ku-band 200-W pulsed power amplifier based on waveguide spatially power-combining technique for industrial applications," *IEEE Trans. Ind. Electron.*, vol. 61, no. 8, pp. 4274–4280, Aug. 2014.

[24] D. M. Pozar, *Microwave Engineering*. Hoboken, NJ, USA: Wiley, 2009.

[25] H. J. Du Toit, D. I. De Villiers, and R. D. Beyers, "A simple low loss partially-filled 16-way radial power combiner," in *IEEE MTT-S Int. Microw. Symp. Dig.*, Jun. 2019, pp. 440–443.

[26] A. Bergquist, "Wave propagation on nonuniform transmission lines (short papers)," *IEEE Trans. Microw. Theory Techn.*, vol. MTT-20, no. 8, pp. 557–558, Aug. 1972.

[27] A. G. Williamson, "Equivalent circuit for radial-line/coaxial-line junction," *Electron. Lett.*, vol. 17, no. 8, p. 300, 1981.

[28] A. G. Williamson, "Radial-line/coaxial-line stepped junction (short papers)," *IEEE Trans. Microw. Theory Techn.*, vol. MTT-33, no. 1, pp. 56–59, Jan. 1985.

[29] K. Song, Y. Fan, and Z. He, "Broadband radial waveguide spatial combiner," *IEEE Microw. Wireless. Compon. Lett.*, vol. 18, no. 2, pp. 73–75, Feb. 2008.

[30] T.-I. Hsu and M. D. Simonutti, "A wideband 60 GHz 16-way power divider/combiner network," in *IEEE MTT-S Int. Microw. Symp. Dig.*, May 1984, pp. 175–177.

[31] R. B. Keam and A. G. Williamson, "Broadband design of coaxial line/rectangular waveguide probe transition," *IEE Proc. Microw., Antennas Propag.*, vol. 141, no. 1, pp. 53–58, Feb. 1994.

[32] A. Tessmann *et al.*, "Metamorphic HEMT MMICs and modules operating between 300 and 500 GHz," *IEEE J. Solid-State Circuits*, vol. 46, no. 10, pp. 2193–2202, Oct. 2011.

[33] M. S. Gupta, "Degradation of power combining efficiency due to variability among signal sources," *IEEE Trans. Microw. Theory Techn.*, vol. 40, no. 5, pp. 1031–1034, May 1992.

[34] A. Keerti and A.-V. H. Pham, "RF characterization of SiGe HBT power amplifiers under load mismatch," *IEEE Trans. Microw. Theory Techn.*, vol. 55, no. 2, pp. 207–214, Feb. 2007.

[35] P. Neininger *et al.*, "Broadband 100-W Ka-band SSPA based on GaN power amplifiers," *IEEE Microw. Wireless Compon. Lett.*, to be published.

[36] P. Neininger, R. Amirpour, L. John, C. Friesicke, R. Quay, and T. Zwick, "A phase shifter with integrated PA MMIC for Ka-band frequencies," in *German Microw. Conf. (GeMiC)*, Mar. 2020, pp. 13–16.

[37] J.-P. Fraysse *et al.*, "A 20W Ka-band radial solid-state power amplifier with 20% associated power-added efficiency," in *Proc. Eur. Microw. Integr. Circuits Conf.*, Oct. 2013, pp. 688–691.

[38] L. W. Epp, D. J. Hoppe, D. Kelley, and A. R. Khan, "Wideband radial power combiner/divider fed by a mode transducer," U.S. Patent 7 385 462 B1, Jun. 10, 2008.

Philipp Neininger received the M.Sc. and the Ph.D. (Dr.Ing.) degrees in electrical engineering and information technologies from the Karlsruhe Institute of Technology, Karlsruhe, Germany, in 2017 and 2021, respectively.

He is currently a Research Associate with the Fraunhofer Institute for Applied Solid State Physics (Fraunhofer IAF), Freiburg im Breisgau, Germany. His research interests include millimeter-wave power combining, integrated circuit (IC) integration and broadband, and high-efficiency power amplifier designs in III–V semiconductor processes for the Ka-band and beyond.

Martin Zink was born in Freiburg, Germany, in 1981. He received the Certified Engineering degree in mechanical engineering from the Deutsche Angestellten Akademie, Karlsruhe, Germany, in 2010.

In 1999, he joined the Fraunhofer Institute for Applied Solid State Physics, Freiburg, where he is involved in the computer-aided design and the microassembly of monolithic microwave integrated circuit modules from 100 MHz to 1.1 THz.

Laurenz John received the Master of Science (M.Sc.) and Ph.D. (Dr.Ing) degrees in electrical engineering and information technologies from the Karlsruhe Institute of Technology (KIT), Karlsruhe, Germany, in 2016 and 2021, respectively.

He is currently an RF Design Engineer and a Project Leader with the Fraunhofer Institute for Applied Solid State Physics (Fraunhofer IAF), Freiburg, Germany. Since 2016, he has been involved in the design and characterization of InGaAs-channel HEMT devices and integrated circuits on GaAs and Si substrates for wireless applications up to 800 GHz. His current research interests include integrated circuit (IC) and package design for radar, communication, and quantum computing applications at millimeter-wave and terahertz frequencies.

Christian Friesicke (Member, IEEE) was born in Berlin, Germany, in 1981. He received the Dipl.Ing. degree in electrical engineering from the Technische Universität Hamburg–Harburg, Hamburg, Germany, in 2008.

From 2005 to 2006, he was a Visiting Scholar with the University of California at Berkeley, Berkeley, CA, USA. From 2008 to 2015, he was with the Institut für Hochfrequenztechnik, Technische Universität Hamburg–Harburg. In 2015, he joined the Fraunhofer Institute for Applied Solid State Physics (IAF), Freiburg, Germany, where he is involved in monolithic microwave integrated circuits (MMIC) design activities. His current research interests are the theory and design of power amplifiers in III–V and GaN technologies.

Axel Tessmann received the Dipl.Ing. and Ph.D. degrees in electrical engineering from the University of Karlsruhe, Karlsruhe, Germany, in 1997 and 2006, respectively.

In 1997, he joined the Microelectronics Department, Fraunhofer Institute for Applied Solid State Physics (Fraunhofer IAF), Freiburg im Breisgau, Germany, where he is involved in the development of monolithically integrated circuits and subsystems for high-resolution imaging systems and high-data-rate wireless communication links. He is currently a Group Manager of the Millimeter-Wave Packaging and Subsystem Group, Fraunhofer IAF. His main research areas are the design and packaging of millimeter-wave and submillimeter-wave integrated circuits (ICs) using high-electron-mobility transistors on GaAs, GaN, and InP as well as circuit simulation and linear and nonlinear device modeling.

Rüdiger Quay (Senior Member, IEEE) received the Diploma degree in physics from Rheinisch-Westfälische Technische Hochschule (RWTH), Aachen, Germany, in 1997, and the Ph.D. degree (Hons.) in technical sciences, the second Diploma degree in economics, and the Venia Legendi (Habilitation) degree in microelectronics from the Technische Universität Wien, Vienna, Austria, in 2001, 2003, and 2009, respectively.

In 2001, he joined the Fraunhofer Institute of Applied Solid-State Physics (Fraunhofer IAF), Freiburg im Breisgau, Germany, in various positions. He is currently the Deputy Director of Fraunhofer IAF, where he is responsible for the business fields. Since 2020, he has been a Fritz-Hüttinger Professor with the Institute for sustainable systems, Albert-Ludwig University, Freiburg im Breisgau. He has authored or coauthored more than 300 refereed publications, three monographs, and contributions to two further.

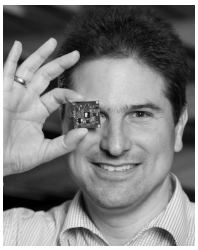

Thomas Zwick (Fellow, IEEE) received the Dipl.Ing. (M.S.E.E.) and the Dr.Ing. (Ph.D.E.E.) degrees from the Universität Karlsruhe (TH), Karlsruhe, Germany, in 1994 and 1999, respectively.

From 1994 to 2001, he was a Research Assistant with the Institut für Höchstfrequenztechnik und Elektronik (IHE), TH. In February 2001, he joined the IBM T. J. Watson Research Center, Yorktown Heights, NY, USA, as a Research Staff Member. From October 2004 to September 2007, he was with Siemens AG, Lindau, Germany. During this period, he managed the RF Development Team for automotive radars. In October 2007, he became a Full Professor at the Karlsruhe Institute of Technology (KIT), Karlsruhe. He is currently the Director of the Institute of Radio Frequency Engineering and Electronics (IHE), KIT. He is the coeditor of three books and the author or coauthor of 120 journal articles, over 400 contributions at international conferences, and 15 granted patents. His research interests include wave propagation, stochastic channel modeling, channel measurement techniques, material measurements, microwave techniques, millimeter-wave antenna design, wireless communication, and radar system design.

Dr. Zwick has been a member of the Heidelberg Academy of Sciences and Humanities since 2017. Since 2019, he has been a member of acatech (German National Academy of Science and Engineering). His research team received over ten best paper awards on international conferences. He served on the technical program committee (TPC) of several scientific conferences. He was the General Chair of the International Workshop on Antenna Technology (iWAT 2013), Karlsruhe, in 2013, and the IEEE MTT-S International Conference on Microwaves for Intelligent Mobility (ICMIM), Heidelberg, in 2015. He was the TPC Chair of the European Microwave Conference (EuMC) in 2013 and the General TPC Chair of the European Microwave Week (EuMW) in 2017. In 2023, he will be the General Chair of EuMW, Berlin. From 2008 until 2015, he has been the President of the Institute for Microwaves and Antennas (IMA). He became selected as a Distinguished IEEE Microwave Lecturer for the period 2013–2015 with his lecture on "QFN Based Packaging Concepts for Millimeter-Wave Transceivers." In 2019, he became the Editor-in-Chief of the IEEE MICROWAVE AND WIRELESS COMPONENTS LETTERS.